

Interplay between Lithium Intercalation and Plating during Fast Charging of Lithium-Ion Batteries Investigated by Operando NMR Spectroscopy

Abdelmounaim Akchach, Pierre-Alain Bayle, Anton Buzlukov, Marion Chandesris,*
Sylvie Génies, and Michel Bardet

During fast charging, metallic lithium can form on the negative graphite electrode, compromising both cycle life and safety. After deposition, plated lithium can re-intercalate within graphite, be disconnected or chemically oxidized. To better understand these reactions and their kinetics, operando measurements on cells with electrochemical performances close to commercial ones are essential. Herein, a dedicated pouch-cell design is developed to follow the dynamic of lithium using ^{7}Li nuclear magnetic resonance (NMR) spectroscopy. These developments provide ^{7}Li NMR spectra every 6 min leading to a good temporal resolution. The dynamics of lithium is investigated for various charging scenarios and temperatures within NMC 811/graphite

pouch cells with industry-standard electrodes. Introduction of an original method allows assessing the mass of plated lithium formed in operando mode, offering insights on the competition between graphite lithiation, plating, and reintercalation processes. Interestingly, the lithium deposition occurs mainly during the constant-current step and early stage of the constant-voltage (CV) step, and lithium reintercalation, oxidation, or disconnection during the subsequent CV hold, highlighting the interest of reducing the current during fast-charge scenario. Comparison with three-electrode monolayer pouch cells provides an onset of plating located between -100 and -150 mV versus Li.

1. Introduction

Rechargeable lithium-ion batteries (LIBs) are a widely used type of battery for various applications, including portable electronics, electric cars, and renewable energy storage systems. Lithium is intercalated into the graphite-based negative electrode during charging at a range of potential between roughly 0.25 and 0.01 V versus Li^+/Li .^[1] This later threshold should not be exceeded because below 0 V the deposition of metallic lithium can occur. Metallic lithium deposition, referred to as the lithium plating phenomenon, occurs at a negative or near zero electrode potential versus Li^+/Li . It leads to cell capacity losses and can induce

dendrites formation with a risk of safety caused by internal short circuits.^[2] Three operational and environmental conditions can lead to negative values of the negative electrode potential: low temperature, high charging C-rates, as well as high cell voltage or high state of charge (SoC) levels, which corresponds to a high state of lithiation of the graphite.^[3,4] This degradation mechanism, occurring under current, is better understood through operando characterization techniques. Indeed, in comparison with traditional ex situ measurements,^[5,6] where the system is removed from its operational environment and studied under static or isolated conditions, the operando measurements give access to the complexity of the reaction dynamics under realistic operating conditions.

In the field of LIBs, operando measurements using the contribution of reference electrode response^[7,8] or advanced characterization techniques based on operando microscopy,^[9,10] X-ray^[11] or neutron diffraction,^[12,13] or Raman and Glow-discharge optical emission spectroscopy^[14] have helped to clarify the complexity of the lithiation processes at the electrode scale in competition with the plating. Nevertheless, quantitative access to the dynamics of plating in competition with graphite lithiation remains very interesting but difficult to access. Among the techniques used to address this question, nuclear magnetic resonance (NMR) stands out. NMR is a nondestructive spectroscopic method that exploits the magnetic properties of atomic nuclei to gain insights into molecular composition, structure, and dynamics.^[15] It has been employed in different ways for battery research. Ex situ or in situ NMR involves analyzing samples taken from the battery (for ex situ) or still in the battery (for in situ) but always outside of its operational context. Ex situ NMR can be carried under

A. Akchach, M. Chandesris, S. Génies
University Grenoble Alpes
CEA-Liten
F-38054 Grenoble, France
E-mail: marion.chandesris@cea.fr

P.-A. Bayle, M. Bardet
University Grenoble Alpes
CEA, IRIG, MEM
38000 Grenoble, France

A. Buzlukov
IMP UB RAS—M.N. Mikheev Institute of Metal Physics of Ural Branch of Russian Academy of Sciences
620137 Ekaterinburg, Russia

 Supporting information for this article is available on the WWW under <https://doi.org/10.1002/batt.202500208>

 © 2025 The Author(s). *Batteries & Supercaps* published by Wiley-VCH GmbH. This is an open access article under the terms of the Creative Commons Attribution-NonCommercial License, which permits use, distribution and reproduction in any medium, provided the original work is properly cited and is not used for commercial purposes.

high-resolution conditions using magic angle spinning (MAS) NMR technique. Performed on powder samples or in very small capsules, it provides high-resolution spectra of solid and has been applied successfully for *ex situ* studies of batteries' components for several decades.^[5,16,17] Nevertheless, MAS NMR technique remains very challenging for *in situ* studies of batteries and very few groups have overcome the numerous problems to be solved.^[18] *In situ* NMR in static conditions allows measurements with a good resolution—even if reduced compared to MAS NMR—at given states of lithiation in the cell environment, however in equilibrium condition, thus falling short of capturing lithiation dynamics under current.^[19,20] Operando NMR takes a step further, providing real-time measurements while the battery is functioning, as close as possible to real-life use.^[21–26] This approach yields crucial data about the battery's responses to different solicitations under various environmental conditions, helping to identify the lithiation dynamics and then optimize battery cells and electrodes. However, the setup of operando experiments remains challenging to have cell designs representative of real cells while being capable to produce NMR spectra with sufficient spectral and temporal resolution. Some *in situ* and operando NMR measurements use plastic cell capsules, as described by Pecher et al.^[27] for their good stability against moisture and air. With a similar setup, Marker et al.^[24] and later Afonso de Araujo et al.^[25] have shown the potential of NMR operando measurements to monitor the dynamics of lithium plating for different C-rates and temperatures. These results have demonstrated the potential of the operando NMR approach, and the challenge is to improve the design of these operando cells to enhance their electrochemical performance in order to provide studies in conditions more representative of real usage and closer to commercial cells. NMR undoubtedly provides large number of different approaches to study LIB. Furthermore, we must keep in mind that due to complexity of LIB components (paramagnetic, conductive, and/or containing quadrupolar nuclei ...), there are considerable number of points that may lead to misinterpretation such as skin effects, bulk magnetic susceptibility effects which can influence the NMR signal.^[28–30]

This article focuses on the investigation of the effect of temperature and cycling conditions on lithium plating dynamics. To that end, we have developed a dedicated pouch-cell design and instrumentation relying on a homemade coil and a specific pouch cell holder. These developments have made it possible to increase the signal-to-noise ratio to obtain sufficiently resolved ⁷Li NMR spectra over short times. Thus, it allows working in operando mode consistent with the duration of the charging process while keeping electrode performances comparable to those of commercial cells. The operando ⁷Li NMR measurements have been carried on LiNi_{0.8}Mn_{0.1}Co_{0.1}O₂ (NMC 811)/graphite full cells with areal loading electrodes around 2.5 mAh cm⁻². This particular battery chemistry is widely used in commercial applications due to its favorable electrochemical properties.^[31] To understand the impact of temperature on battery performance, the study focuses on three distinct operating temperatures: 0, 20, and 45 °C. The changing of charge rates from 0.2 to 2 C provides information on the conditions that trigger and exacerbate lithium plating during fast charge.^[32] Moreover, quantification of reversible and irreversible lithium plating is addressed. This

quantification is made possible through the accurate monitoring of the kinetics of metallic lithium and the use of reference measurements in the same environment. This optimized and robust setup from the cell to the data acquisition methodology allows for a deeper analysis of the electrochemical processes, shedding light on the extent of reversible and irreversible reactions within the studied system.

2. Experimental Section

2.1. NMR Setup

All NMR experiments were performed on a 4.7 T (77.78 MHz ⁷Li Larmor frequency) Bruker Avance NMR spectrometer. The operational NMR setup, as described in Figure 1, comprises an assembly of six essential components. The first part of this assembly is the probe (1) that is the central element for NMR characterization. This probe consists of three fundamental elements: the radio frequency (RF) coil (2), the developed homemade cell compression holder, and the electrochemical cell (3). The 3D-printed plastic homemade cell compressor is important for holding and compressing the electrochemical cell, thereby ensuring good cycling conditions.^[33,34] The second part of the setup contains the essential components for the electrochemical tests. The test bench is a Bio-Logic SP-200 potentiostat. The connection between the cell and the potentiostat is made via shielded cables (four inside the spectrometer and six outside the spectrometer). Cable shielding is important to minimize electromagnetic interference and reduce unwanted noise that could affect current measurements and of NMR spectra acquisition.^[35] Indeed, operando NMR analysis of batteries involves electric currents in magnetic fields, which can lead to electromagnetic interferences affecting NMR and electrochemical measurements.^[36] The electromagnetic noise comes from the current in the NMR RF coil, which interacts with the electrochemical cell circuits connected to the potentiostat. To mitigate these effects, a low-pass filter (5) is added,

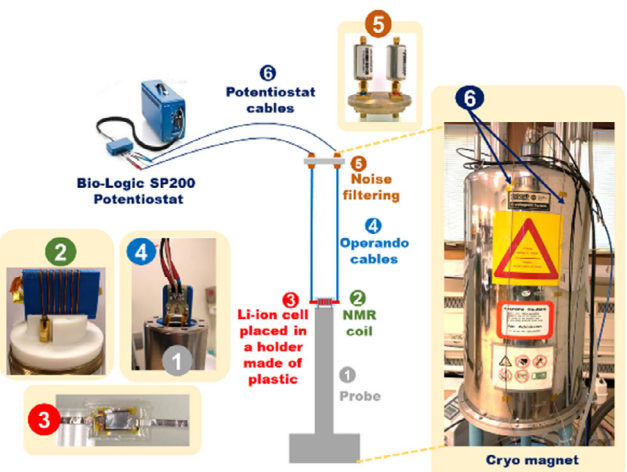


Figure 1. Schematic description of the complete set-up for operando ⁷Li NMR characterization of lithium ion pouch cells.

allowing only low-frequency signals to pass through, while effectively attenuating or blocking higher frequency noise and disturbances, thus improving the signal-to-noise ratio.

The RF coil acts, on the one hand, as a transmitter of radio-frequency pulses and, on the other hand, as a receiver of response from the nuclear spin system. It efficiently transmits the pulses to the sample, inducing resonance on the lithium nuclei, and then captures the resulting NMR reply, providing essential information about the environment and interactions at the atomic-scale level.^[37] To achieve an appropriate RF field, a "homemade" coil was designed according to the experimental requirements and ensure cell dimensions adapted to the NMR probe dimensions. An in-depth simulation study using COMSOL Multiphysics software was carried out to optimize the coil design, ensuring magnetic field uniformity in the measurement area and maximizing NMR excitation and detection efficiency. This approach enables modeling and simulation of the RF coil properties and behavior under various conditions.^[38,39] The simulations were carried out considering the coil geometry and dimensions shown in Figure 2b,c. Parameters such as coil geometry, resonant frequency, electrical, and magnetic properties are taken into account to achieve optimum performance. This approach allows fine-tuning of key parameters, such as coil geometry, number of turns, and material selection, to achieve the optimal magnetic field characteristics.^[40]

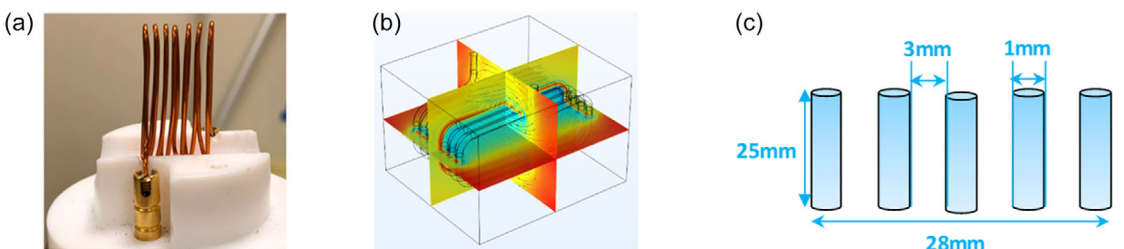


Figure 2. a) RF coil image. b) RF coil geometry used in COMSOL Multiphysics simulations. c) RF coil parameters used in simulations.

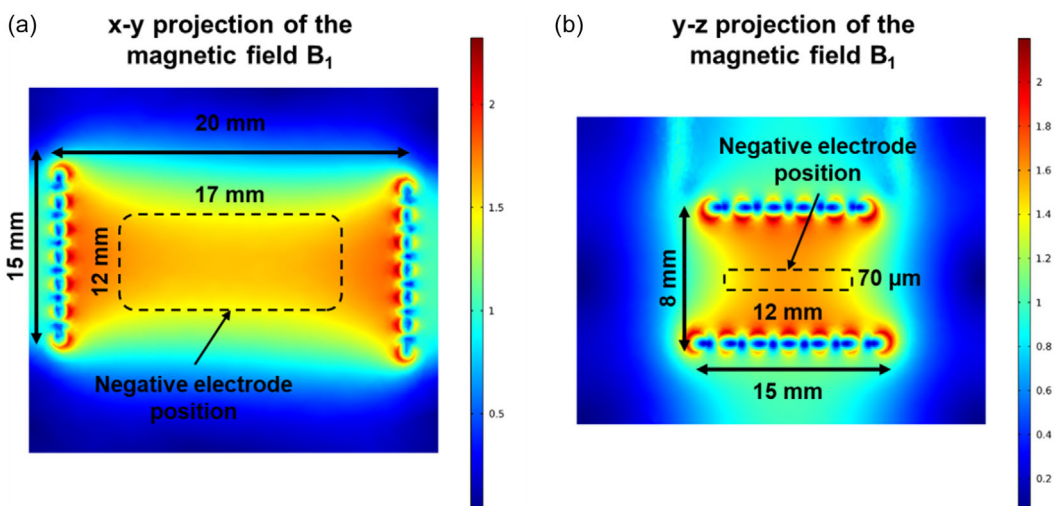


Figure 3. Simulation results for magnetic field B_1 generated by RF coil designed for the 4.7T NMR spectrometer (corresponding to Larmor frequencies of 200 MHz for ^1H nuclei and 77.7 MHz for ^{7}Li). Coil diameter = 2 mm, length = 20 mm and number of coils = 7. a) x-y projection of magnetic field B_1 . b) y-z projection of magnetic field B_1 .

Figure 3a,b displays the 2D projections of the magnetic field distribution generated by the coil, computed using Biot–Savart's law in the x-y and y-z planes. Biot–Savart's law describes the magnetic field produced by a current-carrying wire. The projections onto the x-y and the y-z planes emphasize spatial distribution within these two specific cross sections. Field uniformity is vital for accurate NMR measurements. These projections clearly show the uniformity of the magnetic field, ensuring a homogeneous measurement region. This coherence is crucial for consistent and meaningful results, affirming the coil's reliability and precision. A key simulation result is that, despite the limited number of coil turns (seven in our case), the uniform magnetic field region effectively covers the entire electrode surface. This ensures that the region of interest for measurements or experiments spans the desired area. Complete electrode coverage with a uniform magnetic field is crucial for accurate spatial information.

2.2. ^{7}Li Operando NMR Characterization

2.2.1. Operando NMR Cell

Cell preparation and assembly are conducted entirely in a dry room (dew point at -40°C). The NMC 811 positive electrode contains 96 wt% of $\text{Li}-\text{Ni}_{0.8}\text{Mn}_{0.1}\text{Co}_{0.1}\text{O}_2$, 1 wt% of super P, 0.5 wt% of VGCF, and 2.5 wt% of polyvinylidene fluoride (PVDF) coated on an

aluminum foil for a loading of 14.4 mg cm^{-2} and a thickness of $65 \pm 2 \mu\text{m}$. The graphite-based negative electrode is made of 96 wt% of graphite with 1.3 wt% of Na-CMC (sodium carboxymethyl cellulose), 1 wt% of SC45 carbon black, and 1.7 wt% of latex coated on a copper foil for a loading of 9.5 mg cm^{-2} and a thickness of $69 \pm 3 \mu\text{m}$. The electrodes have been assembled with a trilayer microporous (PP/PE/PP) separator (Celgard 2325, 25 μm thick), leading to a cell-specific capacity around 2.5 mAh cm^{-2} at C/10, 25 °C. The electrodes were cut into rectangular shapes measuring $2.8 \times 1.4 \text{ cm}^2$ for NMC 811 and $3.2 \times 1.7 \text{ cm}^2$ for graphite. The electrodes were dried at 55 °C for 24 h in a dynamic vacuum. Assembled in a ceramic barrier film used as packaging, the cells undergo a second 24 h drying cycle before being transferred to an argon-filled glove box for the cell activation step. This step involves filling the cell with a liquid electrolyte comprising 1 M LiPF₆ in a ternary mixture of ethylene carbonate (EC), dimethyl carbonate (DMC), and ethyl methyl carbonate (EMC) with a volume ratio of 1EC/1DMC/1EMC + 2%wt vinylene carbonate (VC).

The common flexible packaging used for pouch cells has a thickness of 110 μm and consists of three layers: an inner layer of polypropylene (PP), a 40 μm aluminum layer in the middle, and an outer layer of polyamide (PA) (see Figure 4a). The aluminum layer's presence causes a challenge for NMR measurements, as it blocks the RF signals used in NMR experiments.^[41] To overcome this limitation, a ceramic barrier film from Mitsubishi Chemical Gas (MGC) is used as an alternative packaging material. With a total thickness of 115 μm , it comprises three layers: a polyethylene (PE) film on the inner side, a ceramic layer, and a polyethylene terephthalate (PET) film on the outer side. Originally designed for food, pharmaceutical, and electronics industries, this film acts as an effective barrier against moisture and gases for several days, compatible with a cycling protocol of a few days. This has been demonstrated by following the reactivity of a piece of lithium foil encapsulated inside such a pouch over time for five days. Note that finding a good barrier to oxygen and nitrogen gases and steam is the most difficult. This ceramic barrier film not only protects the cell's internal components but also reduces RF shielding caused by the aluminum layer, making it a valuable solution for NMR pouch cell packaging.

2.2.2. Electrochemical Cycling Protocol

Preliminary tests were carried out to fine-tune the NMR sequence, verify with dedicated NMR measurements that possible skin

effects are negligible, and validate the design of the NMR pouch, leading to limited electrochemical cell variability. The electrochemical reproducibility of the NMR pouch was further evaluated by comparing its cycling performance with that of a conventional monolayer pouch cell ($3.2 \times 3.2 = 10.24 \text{ cm}^2$ of positive electrode area) with the same electrodes (see Section 3.1) and instrumented with a reference electrode. Electrochemical cycling tests were conducted at three charging rates (0.2, 1, and 2 C) and three temperatures: 45, 25, and 0 °C while discharge was always performed at a slow current rate of 0.1 C. A different NMR pouch has been used for each tested temperature. Prior to C-rate testing, each cell was formed at C/10 in charge and discharge, at the tested temperature and in the NMR setup. This was done to minimize cell handling, given the sensitivity of the experimental setup. A single formation cycle has been performed to respect gas permeation resistance capabilities of the ceramic barrier film bag used for cell packaging. This formation cycle is a good compromise between experimental constraints and capacity stabilization. For some preliminary tests, the formation step was carried at C/20 in charge and discharge. Voltage cycling ranged from 4.2 to 2.5 V. During charge cycles, a controlled protocol known as CC-CV (constant current–constant voltage) was employed, ensuring a systematic and regulated charging process. The CV step is applied until the current drops below 0.02 C, indicating an almost complete charging process. This protocol is designed to prevent overcharging by gradually reducing the charge current as cell voltage increases.^[42] Precise temperature control was achieved through a controlled flow of compressed air, either heated using the integrated probe's heating element or cooled using a dedicated cooling unit inserted in the magnet of the NMR spectrometer.

2.2.3. NMR Pulse Sequence and Processing

The ⁷Li NMR spectra were acquired using a single-pulse sequence using a direct excitation pulse of 1 μs , a short delay time before acquisition to avoid acquisition of residual signal from the pulse, and a 1 s recycling delay before repetition of the pulse to ensure complete magnetization recovery. The process is repeated 300 times to enhance the signal-to-noise ratio, leading to a complete sequence of roughly 6 min. Pulse sequence and parameters are given in Figure S1, Supporting Information. Such experimental conditions allow us to perform the operando ⁷Li NMR measurements in adequate conditions to monitor any NMR changes induced by the electrochemical cycling effects. The data were

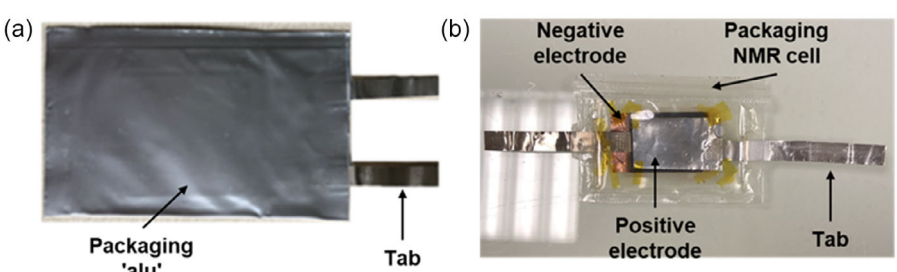


Figure 4. a) Classical pouch cell assembled with standard laminated film with aluminum foil for packaging ($3.2 \times 3.2 = 10.24 \text{ cm}^2$ of positive electrode). b) "NMR" pouch cell assembled with a transparent ceramic barrier film used as packaging ($2.8 \times 1.4 = 3.92 \text{ cm}^2$ of positive electrode).

acquired and processed first with Topspin software from Bruker to transform NMR data from the time domain into the frequency domain. Then the analysis (e.g., spectral deconvolution and quantification) and plotting of the spectra (i.e., NMR vs electrochemical features) are carried out with home-written scripts developed by the authors.

2.3. Quantifying Lithium Plating

To achieve quantitative NMR results regarding lithium deposition under variable conditions, acquiring reference spectra of metallic lithium in the same pouch cell environment as operando experiments is imperative. For this purpose, another experimental cell design has been manufactured, consisting of the assembly of a NMC811/graphite cell containing a disk of lithium of known mass, which was itself encapsulated in a small pouch. All the lithium disks have the same thickness of 50 μm but with different diameters to obtain different masses. This design enables subsequent acquisition of ${}^7\text{Li}$ NMR reference spectra, which reflect real-system conditions, for different known lithium amounts while preventing the metallic lithium–electrolyte reactions (Figure S2, Supporting Information). Quantifying NMR peaks associated with different metallic lithium amount in reference spectra allows establishing a correlation between the observed peak intensity and the lithium quantity. This will provide a calibration law, relating the mass of metallic lithium foil to corresponding NMR signal intensity (see Section 3.5.1).

3. Results and Discussion

3.1. Methodology for ${}^7\text{Li}$ Operando NMR Data Analysis

Figure 5a provides an overview of the distinct ${}^7\text{Li}$ contour plots of operando NMR spectra under different charge conditions. The dataset contains the voltage curve (left) as well as contour plot of the NMR spectra (right). The voltage curve displays the typical features of NMC 811/graphite cells with electrochemical performances similar to those obtained in a classical pouch cell (see Figure S3, Supporting Information). To facilitate readability, pink, orange, and green shading highlight CC–CV charge, rest, and discharge steps, respectively. This convention will be used systematically in this work. Regarding the NMR spectra, each chemical shift corresponds to a specific chemical environment of lithium nuclei. The variations in the contour plots in Figure 5a result from progressively increasing charge rates. In fast charging scenarios, the lithiation process takes place over a shorter period than with slower charging rates. As a result, lithium ions have less time to fully intercalate into the graphite lattice and to diffuse in the electrolyte through the thickness of the electrodes leading to the observed overlap of several resonance signals. To analyze these complex dynamics, a proper assignment of different NMR resonances remains crucial.

Figure 5b focuses on an initial charge and discharge cycle performed at C/20 where the characteristic NMR peaks have been highlighted. To interpret these peaks, caution should be taken

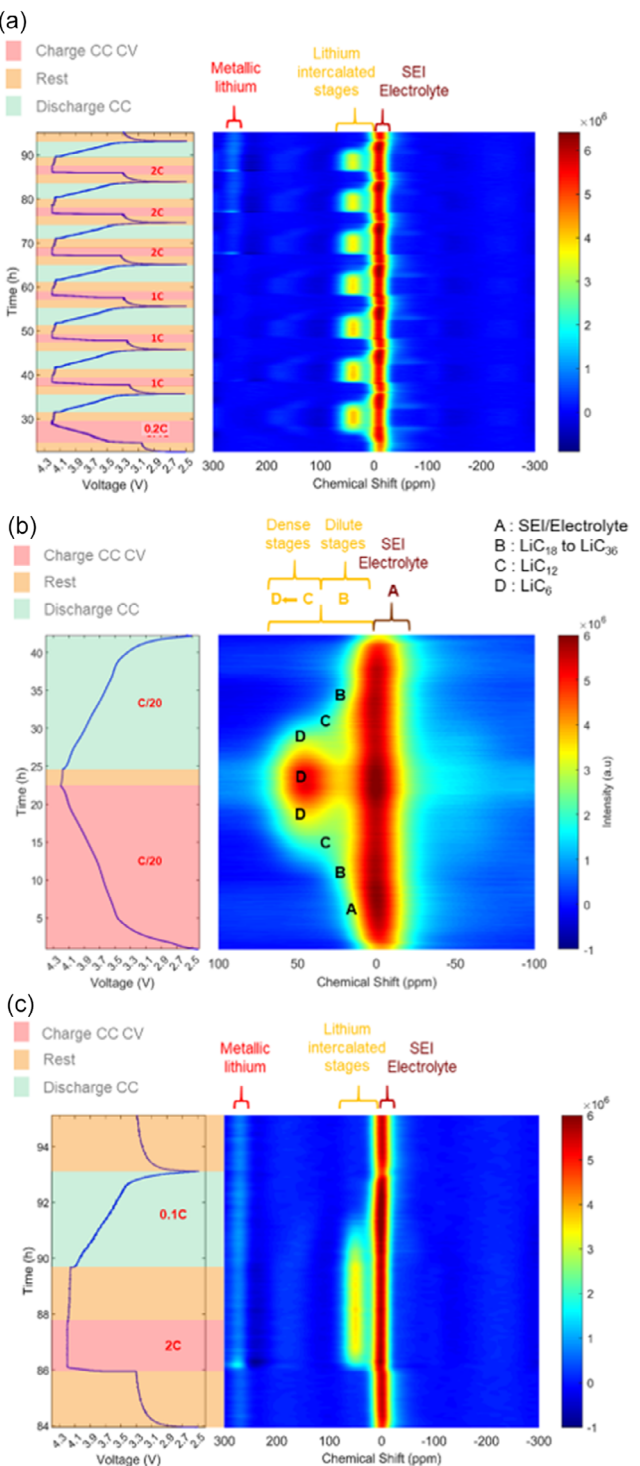


Figure 5. a) ${}^7\text{Li}$ operando NMR results recorded on a NMC811/graphite cell during galvanostatic cycling between 4.2 and 2.5 V at 25 °C: cell voltage profiles at different (dis)charge rates and corresponding ${}^7\text{Li}$ contour plots of operando NMR spectra. b) Zoom on a low cycle: charge and discharge at C/20. The “A” signal corresponds to the lithium ions in the SEI/electrolyte. The “B” signal corresponds to the most diluted intercalation stages (LiC_{36} to LiC_{18}). The “C” and “D” signals correspond to dense LiC_{12} and LiC_6 phases, respectively. c) Zoom on the last cycle: charge at 2 C and discharge at 0.1 C.

when comparing spectra from different laboratories due to some slight variations in the chemical shifts of Li_xC_6 phases documented in the literature.^[43,44] Indeed, the chemical shift value

depends on the graphite lithiation states as well as on the shape and position of the sample within the RF coil. To assign properly the peaks "A," "B," "C," and "D" displayed in Figure 5b, reference NMR spectra of different lithiated graphite electrodes at known states of lithiation were acquired under similar NMR conditions. These spectra are plotted in Figure S4, Supporting Information. The different characteristic peaks "A," "B," "C," and "D" are clearly visible in the range of chemical shifts from 0 to 50 ppm. The signal "A," centered at 0 ppm, was recorded at SoC 0% (delithiated graphite). It is attributed to lithium resonances either of the electrolyte or SEI components.^[45] The spectral area between 10 and 50 ppm is characteristic of lithium intercalated in graphite. It should be recalled that lithium intercalation into graphite occurs through several stages, from 4 to 1, the stages being defined according to the number of host layers that periodically separates two successive intercalant layers.^[46–49] The ⁷Li NMR signal changes between the different stages, especially, it is usually possible to distinguish between the denser and more dilute stages. The signal "B" (in the range between 10 and 25 ppm), clearly visible for the sample at SoC 50%, corresponds to the most diluted intercalation stages with partial occupancy of lithium sites between the graphite layers (LiC₃₆ to LiC₁₈). This signal is indicative of the early stages of lithiation.^[24,50,51] For higher graphite lithiation states (cell at SOC 100%), other peaks ("C" and "D") appear in the range of 25–50 ppm. They are attributed to denser Li_xC₆ phases where the occupied layers are filled with more lithium. A particularly prominent feature is the NMR signal at a chemical shift of 49 ppm designated as "D" in Figure 5b and S4, Supporting Information. This resonance corresponds to the central transition line ($m_l = -1/2 \leftrightarrow +1/2$) of the ⁷Li nuclei in LiC₆.^[22] In addition, as shown in Figure S4, Supporting Information, besides this line there are also two satellite lines corresponding to $m_l = \pm 3/2 \leftrightarrow \pm 1/2$ quantum transitions of this nuclei with spin $I = 3/2$.^[6] Asterisks label these satellites. The LiC₁₂ phase designated as "C" in Figure 5b and S4, Supporting Information, has a distinct chemical shift of 45 ppm.^[50,51] This shift reflects the different electronic environment of lithium ions in LiC₁₂ compared to LiC₆, due to a different bonding configuration. In conclusion, signals from the most dilute stages (peak "B") are observed in the chemical shift range from 10 to 25 ppm, while signals from denser Li_xC₆ phases (peaks "C" and "D") appear in the range of 25–50 ppm.^[51]

Figure 5c shows the operando NMR results during a cycle at a particularly high charge rate of 2 C. The ⁷Li NMR spectra exhibit the same features between 0 to 50 ppm as observed previously for slower charging. However, the most remarkable feature is the appearance of a supplementary contour plot at a distinct chemical shift of ≈ 260 ppm. This signal can be associated with the presence of lithium metal deposited at the negative electrode.^[52] The presence of this "lithium metal" NMR signal in the operando NMR spectrum offers direct, real-time insight into the onset of lithium plating, and provides monitoring of deposition kinetics as a function of cycling conditions. To quantitatively follow the dynamics of lithium metal, the intensity of this peak will be integrated in the range 250–300 ppm.

Note that the signal from ⁷Li of NMC does not appear. Indeed, it gives a very broad signal, whose intensity (spread over a wide spectral range) is rather weak at each specific frequency. Much

higher number of scans is required to acquire this spectrum with comparable signal-to-noise ratio. Thus, the developed experimental setup enables operando monitoring of (dis)appearance of both dense and dilute lithium/graphite phases during cycling, as well as potential lithium metal deposition. As the electrochemical performances are representative of commercial cells, we will apply this methodology to analyze the graphite lithiation and lithium plating dynamics at different temperatures and C-rates in the following sections.

3.2. Temperature Dependence of Graphite (De)-Lithiation Dynamics

In this section, we investigate the influence of temperature and charging rate on the lithiation and delithiation dynamics of the graphite electrode. Typical NMR spectra acquired in operando mode are displayed in Figure S5, Supporting Information. Focusing on the NMR signal intensity between 0 and 50 ppm, we can observe the dilute stage appearance as a shoulder of the electrolyte peak around 15 ppm, followed by a peak at higher ppm values, between 35 and 50 ppm, typical of the denser stages. In this operando mode, the signals of the different stages are less fine than in the ex situ configuration, and the decomposition between all the stages is not achievable. The decomposition was therefore performed assuming two contributions apart from the electrolyte one, one from the more "dilute" stages around 10–25 ppm and one from the denser phases, with a contribution around 25–50 ppm. This quantification enables tracking the progression of lithiation and delithiation within the graphite electrode during the cycling.

Figure 6 displays the results obtained at 0, 25, and 45 °C for different charging rates. The top subfigures show the cell voltage profiles as a function of time while highlighting the different steps of the cycling protocol (charge, rest, and discharge). The bottom sub-figures focus on the graphite (de)-lithiation dynamics. The results show consistent and comparable patterns evolution during charging and discharging cycles throughout the cell cycling process. This observation suggests that the cell maintains stable performance over an extended period, covering several days of continuous cycling. Furthermore, the similarity and reproducibility of the NMR results observed at both low and high charge rates highlight the robustness and adaptability of the setup, which guarantees reliable and accurate NMR measurements under a variety of operating conditions.

As soon as the charge current is applied, the NMR signal intensities progressively rise, starting with those corresponding to the more dilute phases, followed closely by the intensity of the denser stages. After a given time, which depends on the temperature and charging rate, the contribution corresponding to the more "dilute stages" stabilizes, while the NMR signals originated from the dense Li_xC₆ phases continue to increase until the end of the CC step. Due to the resolution and the chosen decomposition approach, no clear decrease in the more "dilute stages" is observed. Throughout the CV step, the evolution of the intensities remains negligible in accordance with the strong decrease of the current. During the discharge, a symmetric scenario is observed.

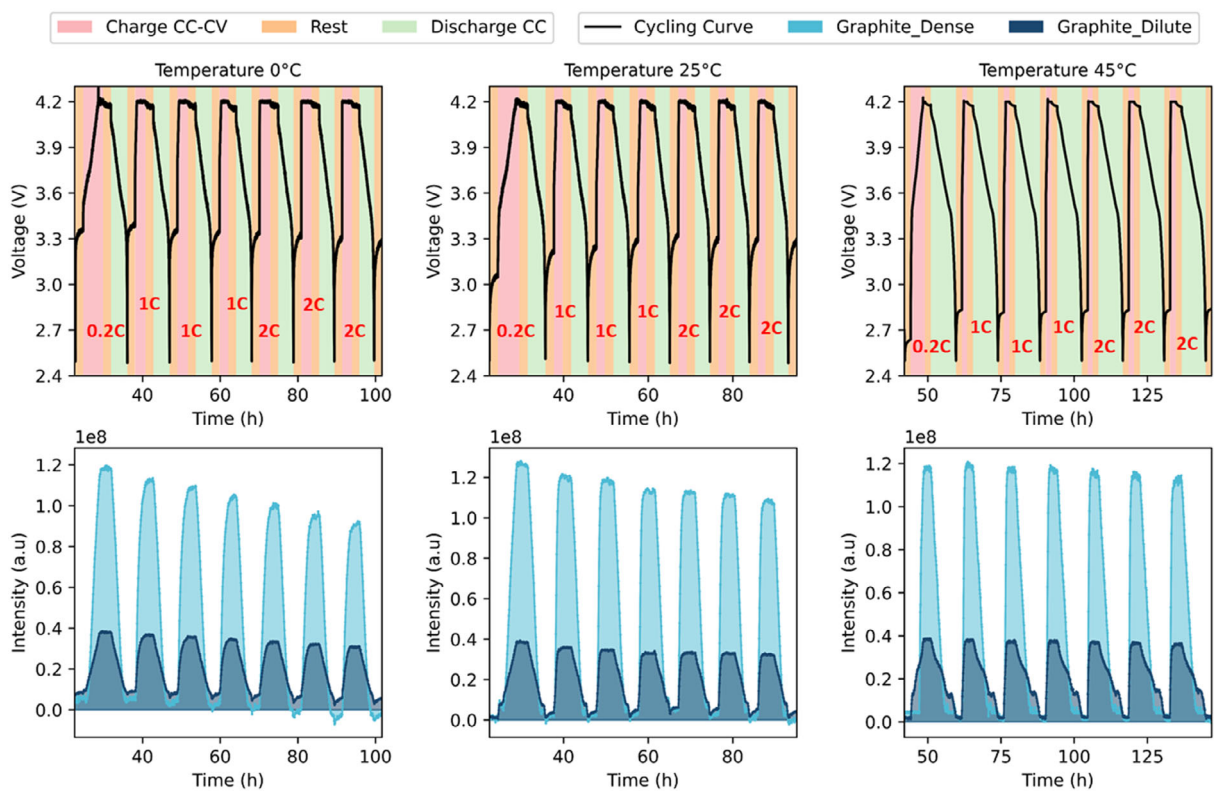


Figure 6. Dynamics of graphite (de)-lithiation during cycling of three different cells at 0, 25, and 45 °C. Top: cell voltage profiles; bottom: evolution of integrated signal intensities of graphite obtained by decomposition of the “dilute” and “dense” graphite contributions.

A comparison of the results acquired at three different temperatures provides insights into the effect of temperature on graphite lithiation. At a relatively high temperature (45 °C), the maximum intensity of dense and dilute lithium/graphite phases remains almost unchanged across all charging rates. This is coherent with a lithiation process facilitated by temperature, resulting in a same final state of lithiation of the graphite electrode, whatever the studied C-rate. Indeed, the higher temperature facilitates the lithium diffusion into the graphite bulk, its transport in the electrolyte, and the kinetics of the electrochemical reaction. As a result, at higher temperatures the lithiation process remains not very sensitive to the variations in the charging rate, indicating a very good cell performance. At 25 °C and high charge rates, a slight decrease in the maximum intensity of the signal from dense phases is observed. This decrease is even higher at 0 °C and can be ascribed to a lower lithiation state at the end of charge. The onset of the denser stages seems to be slightly delayed at 45 °C, compared to lower temperatures. However, given the difficulty of deconvoluting the dilute and dense contributions in operando conditions, we will not draw definitive conclusions beyond the macroscopic evolution of these quantities.

3.3. Temperature Dependency of Lithium Plating

In this section, we investigate the influence of charge rate and temperature on lithium plating formation by monitoring of its kinetics by means of ⁷Li operando NMR. To focus on the chemical shift range associated to metallic lithium,^[53] the intensity of the

NMR spectra was integrated in the range 250–300 ppm. Figure S6 and S7, Supporting Information, illustrate NMR spectra obtained for charges at various C-rates, at 25 and 0 °C, showing the evolution of the peak associated with metallic lithium. **Figure 7** shows the obtained results, with the cell voltage profiles recalled on the top panel to follow the electrochemical sequence, and the integrated “lithium metal” intensity as a function of time on the bottom panel.

One of the main observations in Figure 7 is the absence of any lithium plating during the cycling experiment at 45 °C. This result is consistent with the literature data,^[54–56] which suggests that lithium plating is less likely to occur at higher temperatures. The increased lithium mobility in the electrolyte and its facilitated diffusion into the active material reduce the electrode polarization at higher temperatures and thus favor the graphite lithiation rather than the formation of lithium metal deposit. The constant NMR signal intensities of dense and dilute graphite phases throughout cycling at 45 °C (see Figure 6) are also consistent with a negligible parasitic reaction.

Figure 7 also shows the results obtained at 25 and 0 °C. At low charging rates (0.2 C), no lithium deposition is detected at any of these temperatures. This observation can be attributed to the relatively slow charging rate, which reduces the transport and transfer limitations. The limited polarization of the negative electrode favors graphite lithiation compared to metallic lithium deposition, even at 0 °C. At higher charge rates (1 and 2 C), the transport and transfer limitations become more important, enhancing the electrode polarization. This decrease of negative

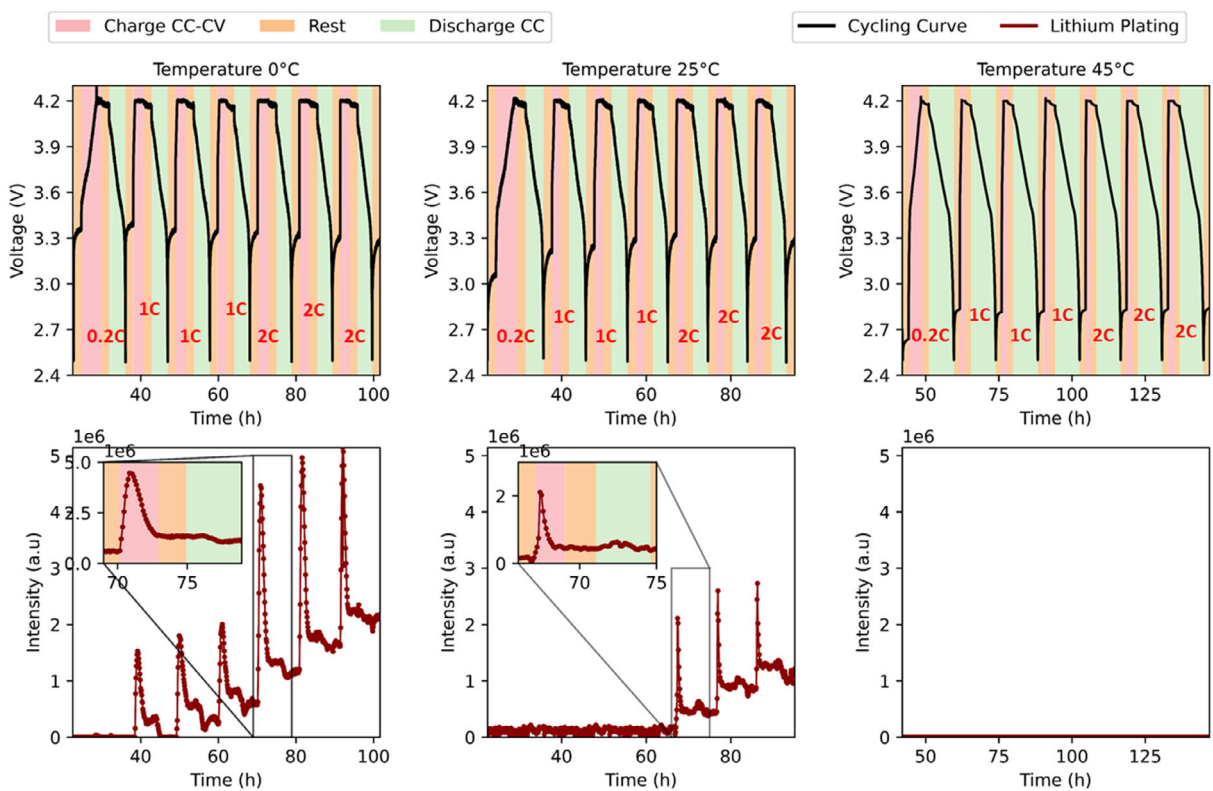


Figure 7. Dynamics of lithium plating during cycling of three different cells at 0, 25, and 45 °C. Top: cell voltage profiles; bottom: integrated "lithium metal" signal intensity. Insert: Intensity for the first cycle at 2 C-D/10.

electrode potential creates favorable conditions for lithium plating, which starts to appear with charge rates of 1 C at 0 °C and 2 C at 25 °C. The insets of Figure 7 focus on the plating dynamics at 2 C at 0 and 25 °C. To further explore the interplay between lithium intercalation and plating/stripping processes, Figure 8 displays the normalized NMR signal intensities corresponding to lithium in graphite (light blue) and metallic lithium (red), alongside the cell potential (black) and the applied current (blue) for the cells cycled at these two temperatures.

During the constant current period, a fast increase of the metallic lithium intensity is observed. The onset of this plating occurs almost simultaneously with the graphite lithiation, except for the first cycle at 1C – 0°C, where a slight delay is observed. These results show that lithium plating occurs in parallel with the intercalation process. This is also visible in the raw NMR spectra of Figure S6 and S7, Supporting Information. The increase of the metallic lithium intensity continues during the early stages of the CV step, and then decreases as the current decreases. Interestingly, this decrease occurs at similar current for the different cycles, around 5 ± 0.5 mA at 25 °C and 2.5 ± 0.3 mA at 0 °C, corresponding to regime of roughly C/2 and C/4 respectively. This observation suggests the existence of a critical current threshold below which lithium plating becomes thermodynamically or kinetically unfavorable. The fact that this threshold current scales with temperature (approximately C/2 at 25 °C and C/4 at 0 °C) is consistent with the expected temperature dependence of lithium diffusion and reaction kinetics. At lower temperatures, the reduced ionic mobility and slower interfacial charge transfer shift the plating/intercalation balance.

During the CV period, lithium ions continue to intercalate into the graphite, but at a slower rate, as can be seen on the light blue curves of Figure 8. Maintaining a constant voltage ensures that the driving force for lithium-ion insertion remains, but the slower rate of intercalation allows overcoming the kinetic limitations. The decrease of current during the CV step reduces the electrode polarization such that the plating conditions are no longer fulfilled, once the polarization is sufficiently low. The decrease in metallic lithium intensity during the CV charge can be attributed to the reaction of deposited lithium with its environment. During the CV step, it can be due to the intercalation of the deposited lithium in the graphite bulk (spontaneous Li-insertion into graphite^[14]), or to the irreversible oxidation reactions of metallic lithium with the electrolyte. At 0 °C, the increase of the lithiated graphite intensity at the end of the CV phase, when the current is very low, concomitant with the strong decrease of the lithium metallic signal, is a sign of reintercalation of metallic lithium into graphite. However, a precise analysis of the involved quantities is not possible, as the lithiated graphite signal remains qualitative but not quantitative in terms of the quantity of lithium intercalated. At the end of the CV step, the metallic lithium intensity stabilizes at a value that can be different from that at the beginning of the cycle. This difference is attributed to the "dead lithium"^[57]: an island of lithium metal electrically isolated from the electrode or partial oxidation of metallic lithium with the electrolyte. These two phenomena are reported in the literature as irreversible plating. NMR enables quantification of dead metallic lithium only. If electrochemically active lithium metal is still present at the end of

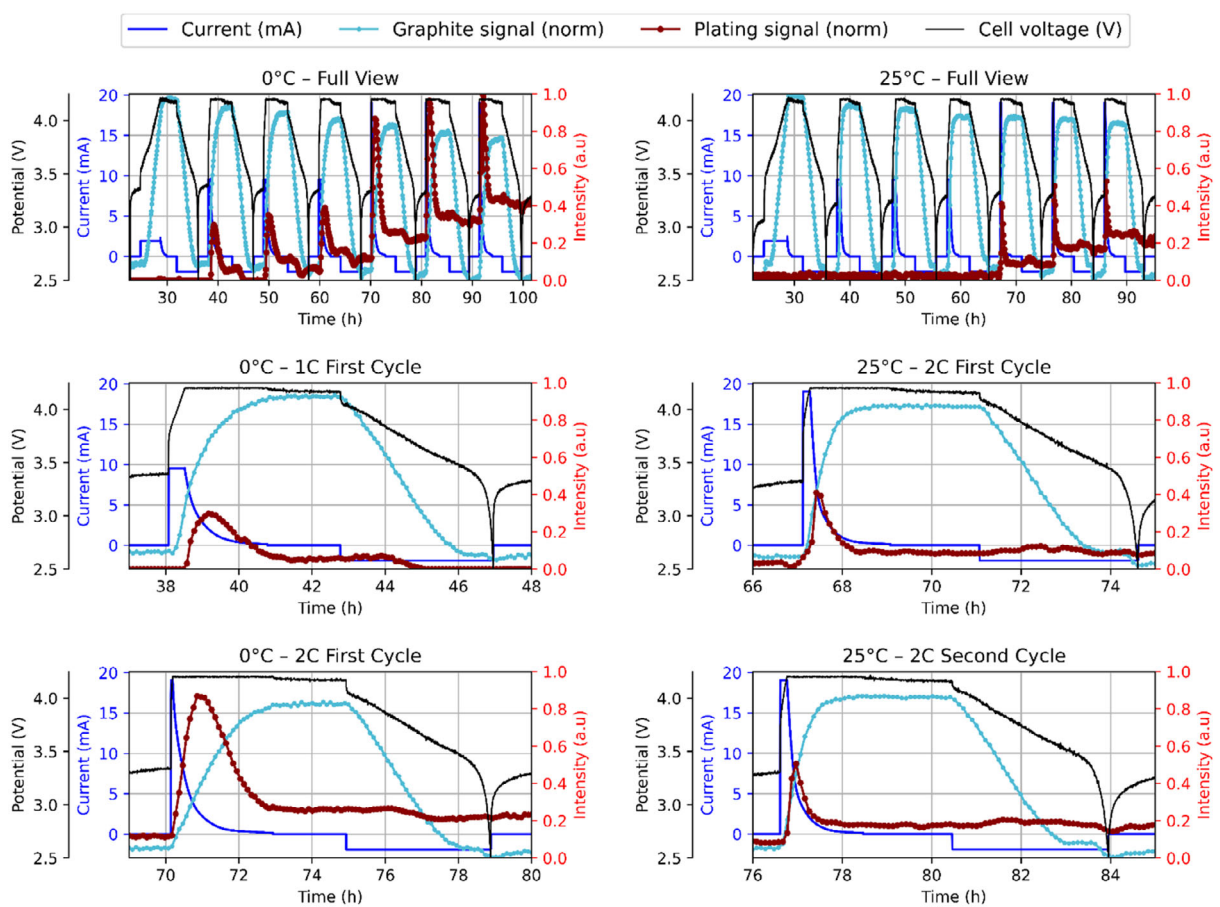


Figure 8. Interplay between lithium intercalation in graphite and lithium plating during cycling of the two different cells at 0 °C (left) and 25 °C (right). Each figure displays the applied current in mA (blue—left axis), the cell potential in V (black—left axis), the normalized sum of the dense and dilute integrated signal intensities of lithiated graphite (light blue—right axis) and the normalized integrated signal intensity of the metallic lithium. For each temperature, a full view of the sequence is displayed on the top, and zoom on two distinct cycles are presented below. For the normalized intensities of the NMR signals, the maximum value of the two experiments is used to facilitate comparison between the two temperatures.

the CC–CV charge, it can be electrochemically reoxidized during the subsequent discharge.^[58] In the present work, we will use the term “reversible plating” for metallic lithium that remains electrochemically active. In the studied conditions, lithium plating is almost never completely reversible. Moreover, the intensity of NMR signal originated from metallic lithium increases in steps, thus the amount of this dead lithium increases with each cycle, and this increase is greatest at 0 °C.

Interestingly, while Märker et al.^[24] reported that lithium plating predominantly occurs during the CV step, our results indicate that, under the studied conditions and with our electrode/cell design, lithium plating can also start during the CC phase. Lithium stripping occurs during the second part of the CV phase, once the current is sufficiently low, and the reversible lithium seems to be fully intercalated into the graphite at the end of the CV period, contrary to the modeling results of Lüders et al.^[59] This suggests that the reduction of current during the charge remains an interesting strategy to favor reintercalation of plated lithium, as long as the performance of electrode is not too much degraded. As the temperature decreases, the onset of plating occurs at a lower current, in coherence with reduced Li-ions mobility and transfer.^[60,61] Furthermore, slower kinetics at

lower temperatures clearly extend the duration of subsequent lithium stripping during the CV period as can be seen from Figure 8. During the subsequent rest and discharge periods, the metallic lithium intensity remains rather constant.

3.4. Onset of Lithium Plating

Plating is thermodynamically favorable when the negative electrode potential reaches 0 versus Li⁺/Li.^[62] However, a potential below zero is not a sufficient condition: in several experiments onset of plating has been reported to occur at negative potential below –100 mV, indicating that the onset of plating occurs far from equilibrium.^[63–65] Simultaneous access to the negative electrode potential and monitoring of plating dynamic is highly desirable, but experimentally very challenging. In the present work, we have performed an indirect correlation, using the results of monolayer pouch cells with the same positive and negative electrodes and instrumented with a reference electrode (see Section S3, Supporting Information).

Thanks to the reference electrode of the classical pouch cell, we have access to the potential of the negative electrode for similar regime and temperature (blue line of Figure S3b, Supporting

Information). The minimum value is reached at the end of the CC step. The experiments have been performed on three different three-electrode cells at each temperature, which gives a dispersion of the potential of the negative reached at the end of the CC step. At 45 °C, the potential of the negative electrode stays above 0 V versus Li at C/5 regime ($+62 \pm 3$ mV vs Li) and is close to 0 V versus Li at 1C (17 ± 25 mV vs Li), in coherence with the absence of plating in the NMR analysis. At 2C, the potential of the negative electrode reaches -68 ± 45 mV versus Li. However, it seems to be not low enough to cause plating, as shown by NMR analysis. At 25 °C, the negative potential reaches $+39 \pm 4$ mV versus Li at C/5 regime and falls below zero from a regime of 1C (-91 ± 24 mV vs Li), even though no plated lithium is observed in the NMR results at 1C. At 2C, the over polarization of the negative is larger, reaching -143 ± 12 mV versus Li, while plating is observed in the NMR results. At 0 °C, the negative potential always drops below zero, reaching -5 ± 2 mV versus Li at C/5, -165 ± 32 mV versus Li at 1C, and -242 ± 35 mV versus Li at 2C, while plating is observed at both 1 and 2C regimes. The onset of plating is therefore not only correlated to the drop of the negative potential below 0 V versus Li, but seems to require an activation threshold below roughly -100 mV versus Li.

To better correlate the onset of lithium plating with the negative electrode potential, we further compare NMR and three-electrode classical pouch cell results. Specifically, we extracted the voltage of the NMR pouch cell at the moment when the lithium metal signal first appears and aligned it with the electrochemical voltage profile of the instrumented three-electrode cell operated under identical C-rate and temperature conditions to determine the value of the negative electrode potential corresponding to the onset of lithium deposition. This indirect comparison is possible only if plating appears during the CC step, which corresponds to the 1C-0 °C and 2C-25 °C conditions. In these cases, the NMR cell potential at plating onset is provided together with the corresponding potential of the negative electrode in Table S1, Supporting Information. The negative potential values are provided when metallic lithium is detected and also 6 min before, to take into account the temporal resolution of the NMR spectra recording. For both temperatures, the onset of plating occurs at a negative potential well below zero, around -136 mV versus Li (-130 mV ± 27 vs Li@2C-25 °C and -143 mV ± 55 vs Li@1C-0 °C). These values should be interpreted with caution, given the 6 min temporal resolution of NMR used to detect the onset of plating and the indirect nature of the correlation.

3.5. Quantification of Lithium (Ir)Reversible Plating

3.5.1. Quantification from NMR Results

The NMR results provide insights into the dynamics of metallic lithium plating/stripping. To go further in the analysis, the intensity of the "lithium metal" NMR peak (in the range of 250–300 ppm) must be correlated with the mass of metallic lithium. To that end, a linear regression law is determined based on the calibration data correlating ^{7}Li NMR signals intensity with known lithium metal

masses (see Figure S8, Supporting Information). This calibration is performed using the experimental cell design presented in Section 2.3. We must also keep in mind that the NMR approach relies on the ability of the RF field to penetrate bulk lithium metal, which can remain limited to the surface. This is known as the skin-depth effect. The value of the skin depth, d , can be estimated, as it depends on known physical constants.^[28] In the present study, $d \approx 14.7$ μm given the Larmor frequency of 77.8 MHz. The calibration samples consist of lithium disks with the same thickness of 50 μm, meaning that lithium masses and lithium surfaces are proportional. This choice also ensures that the NMR signal intensity of the calibration experiments reflects changes of the samples surface rather than being influenced by the penetration limits. Nevertheless, as the thickness of our samples is larger than twice this penetration depth, we estimate that only 60% of the sample is excited by the RF field in this calibration experiment and apply a prefactor of 0.6 to the slope of the linear regression law (see Section S5, Supporting Information). For the NMR conditions and protocol of the study, and for masses of lithium between 0.2 and 1 mg, the law appears almost linear (see Figure S8, Supporting Information), allowing a reasonable correlation. The use of this law also assumes that the lithium metal deposit during the experiments remains below the penetration length and should provide reasonable quantification of the order of magnitude of the deposited lithium mass.

The total mass of metallic lithium plated during a charge is provided by the difference between the maximum and the initial mass value at the beginning of the cycle. Reversible plating refers to the formation of lithium metal on the negative electrode during charging, which can be fully reconverted to lithium ions during CV, rest steps, and/or subsequent discharge. Irreversible plating, on the other hand, occurs when metallic lithium cannot be fully reconverted to lithium ions during subsequent cycling. It can either be oxidized, or remain as dead metallic lithium as illustrated in Figure 9. Therefore, the difference between the maximum value of a given charge and the minimum value measured at the end of discharge is the sum of reversible plating and oxidized metallic lithium. The difference of metallic lithium amount between the end of discharge and beginning of the cycle corresponds to the dead lithium.

Figure 10 shows the results based on the "lithium metal" NMR signal intensity presented in Figure 7. This figure displays for each cycle the masses of 1) total deposited lithium, 2) the sum of the reversible and oxidized lithium, and 3) the amount of dead lithium for the two pouches cycled at 25 and 0 °C, respectively. As can be seen, the total amount of metallic lithium increases with decreasing temperature or increasing charge rate. At 25 °C, the amount of lithium deposited during the three cycles at 1C is negligible, with no dead metallic lithium detected. During the three cycles at 2C, the amount of plated lithium remains rather constant. The dead lithium appears at the first cycle. Its amount slightly decreases over the cycles and corresponds roughly to 18.5% of the total deposited lithium, leading to an accumulation of metal deposition over the three cycles. At 0 °C, the onset of lithium plating starts at 1C with a total amount comparable to that one found at 2C at 25 °C: 0.27 mg at 0 °C – 1C versus 0.31 mg at 25 °C – 2C. At higher charge rate, the amount of

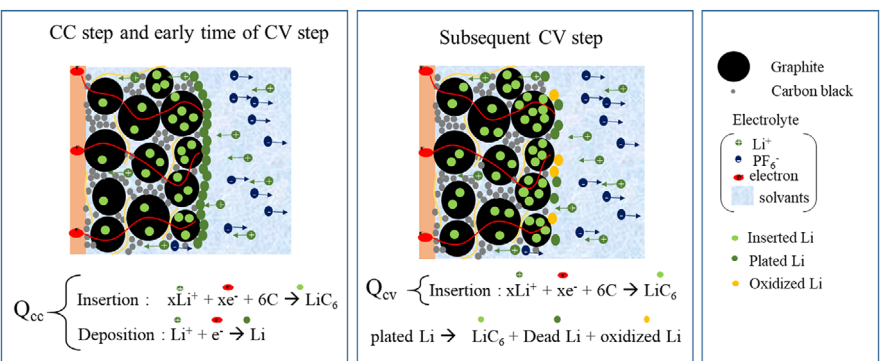


Figure 9. Illustration of the different electro-chemical mechanisms occurring during the constant current and constant voltage steps of the charge.

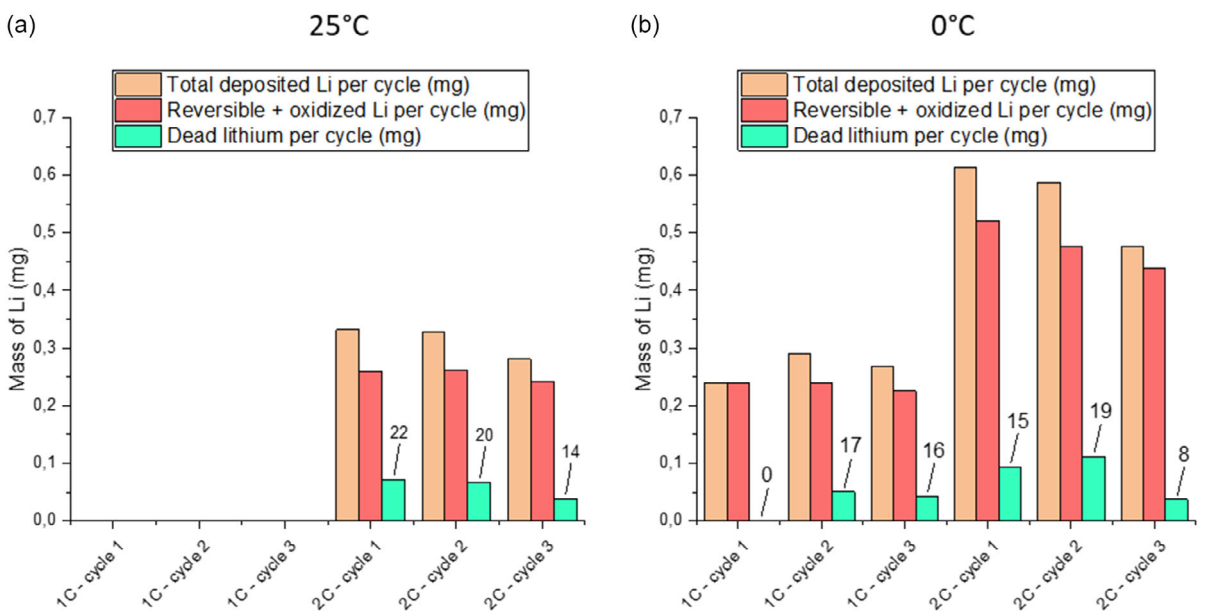


Figure 10. NMR quantification for each cycle of the total deposited lithium, the sum of the reversible and oxidized lithium and the dead lithium for two different NMC811/graphite cells cycled at a) 25 °C and b) 0 °C. The ratio of dead lithium over the total deposited lithium is also presented in percentage in the graph.

deposited lithium nearly doubles (roughly 0.48 mg at 0 °C – 2 C), remaining nearly constant over the subsequent cycles. At 0 °C, the dead lithium appears only after the second cycle at 1 C, while it is present from the first cycle at 2 C. The amount of dead lithium slightly decreases throughout the cycles, but remains approximately around 16%. This ratio is slightly lower than that found at 25 °C, showing a better re-intercalation of plated lithium. This may indicate a slowing down of parasitic reaction kinetics at lower temperature. Even if we observe more plated lithium at this low temperature, it is globally better reintercalated in %, although at a slower rate. Interestingly, the amount of reversible lithium remains very stable over the cycles at similar C-rates.

3.5.2. Correlation with Electrochemical Data

In order to consolidate the analysis, the deposited lithium masses measured by NMR are compared with the quantities of lithium electrochemically exchanged during the cycles. More specifically,

we quantify the exchanged lithium capacity during the charge, distinguishing between the periods of charge at constant current, Q_{CC} and constant voltage, Q_{CV} . These capacities Q are converted into lithium mass using Faraday's law, assuming an insertion reaction involving one mole of electrons per mole of lithium.

$$m_{\text{Li}} = n_{\text{Li}} M_{\text{Li}} = \frac{Q}{F} M_{\text{Li}} \quad (1)$$

where F is the Faraday constant, equal to 26 800 mAh/mol, and M_{Li} is the lithium molar mass, equal to 7 g mol⁻¹. This conversion indicates that each milliampere-hour (mAh) of electrical charge corresponds to ≈260 µg of lithium. This order of magnitude is in coherence with literature, which reports that a 2 Ah cell contains around 0.6 g of lithium.^[66] In our experiments, lithium plating occurs only during the CC step. The electrochemical capacity exchanged during this step has two origins: lithium intercalated in graphite bulk and lithium deposited in metallic form on graphite surface. At constant voltage, the electrochemical capacity

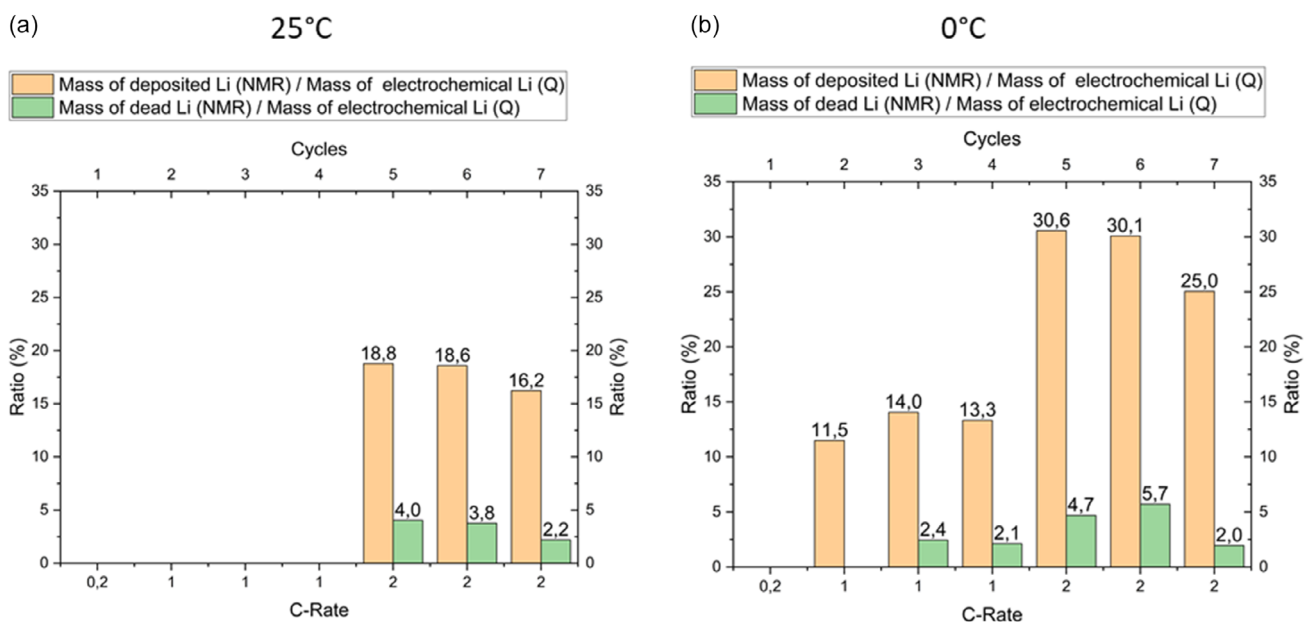


Figure 11. Quantification for each cycle of the ratio of the mass of metallic lithium deposited at its maximum (orange) and of the new dead lithium (green) over the total mass of lithium electrochemically exchanged during the charge for the two different NMC811/graphite NMR cells cycled at a) 25 °C and b) 0 °C.

corresponds only to intercalated lithium. Indeed, during this period the reversible fraction of plated lithium reintercalates into graphite (remaining electrochemically invisible), while an irreversible fraction remains on the electrode surface, being mostly in electrochemically disconnected metallic form. It is therefore relevant to compare the total mass of “electrochemical” lithium exchanged during the CC step, $m_{\text{Li}, Q_{\text{CC}}}^{\text{elec}}$, with that obtained from ${}^7\text{Li}$ NMR. These different quantities are presented in Table S2 and S3, Supporting Information. During the CC step, the charging capacities Q_{CC} show a clear decreasing trend in values as charge rates increase from 0.2 to 2 C, resulting, as expected, in a shorter time before reaching the cutoff voltage. A more insightful approach is to look at the ratio between the total mass of metallic lithium deposited at its maximum and the total mass of lithium electrochemically exchanged during the charge. These ratios are presented Figure 11. It is around 18% for the charge at 2C and temperature 25 °C, 13% for 1 C – 0 °C, and reaches more than 30% for the 2 C – 0 °C conditions. Even if the ratio of dead lithium over the total deposited lithium is slightly higher for 25 °C than for 0 °C at the same charge rate of 2C, the percentage of dead lithium over the total exchange capacity, also plotted Figure 11, remains in the same order of magnitude, around 3–4% for the two temperatures. This shows that the reversibility of the lithium plating (related to the total exchanged capacity) does not strongly depend on the temperature. The irreversible capacities for each cycle are also presented in these Table S2 and S3, Supporting Information. The values for the first cycle at 0.2 C are rather high (~6% at 25 °C and 3.2% at 0 °C). As it is the first cycle after cell formation (see Figure S9, Supporting Information), the capacity is not still fully stabilized. The lower values observed in subsequent cycles illustrate the good electrochemical performance of our

“NMR” pouch cell and confirm the reversibility of the plating deposits.

4. Conclusion

Operando ${}^7\text{Li}$ NMR analysis is a powerful technique for understanding the complex phenomena within LIBs. In the present study, we demonstrate its ability to provide real-time and detailed insights into the intricate processes occurring within the battery during electrochemical cycling. More specifically, it sheds light on the interplay between graphite lithiation and lithium plating in industry-standard electrodes with areal loading around 2.5 mAh cm^{-2} . The good temporal resolution of the measured NMR spectra combined with the good electrochemical performances of the “NMR” pouch cells has been achieved thanks to specific developments in both cell design and NMR setup. The ${}^7\text{Li}$ NMR signals have been acquired during electrochemical cycling from 0.2 C, up to 2 C and at different temperatures between 0 and 45 °C, providing access to graphite lithiation and metallic lithium dynamics at the same time. Classically, at elevated temperatures, the absence of lithium plating aligns with enhanced mobility of lithium ions, favoring the lithiation process, while lower temperatures and higher charging rates lead to plating.

The obtained results further show the concomitant plating and graphite intercalation during either the CC step and/or the early stage of the CV step of the charge. When the current becomes sufficiently low during the CV period, spontaneous reintercalation of metallic lithium into graphite is observed. Interestingly, the decrease in lithium metal intensity occurs at similar current for the different tested regimes, around $5 \pm 0.5 \text{ mA}$ at 25 °C and $2.5 \pm 0.3 \text{ mA}$ at 0 °C, corresponding to regime of roughly C/2

and C/4, respectively. This highlights a current-dependent transition between plating and re-intercalation regimes.

With our cell design, the lithium plating occurs mainly during the CC step of charge, or early phase of the CV step, while the lithium reintercalation, oxidation, or disconnection occur mainly during the subsequent CV step. These findings suggest that reducing the current during the charging could be a good strategy to favor the reintercalation of plated lithium and limit irreversible capacity losses.

To further investigate the onset of plating, we compared the NMR pouch cell plating results to the negative potential measurements from three-electrode monolayer pouch cells. Although the correlation is indirect, it provides valuable insight: plating occurs for cells where the negative potentials go below -100 mV. From this approach, we further estimate an onset of plating around -130 mV ± 27 versus Li@2 C-25 °C and -143 mV ± 55 versus Li@1 C-0 °C. These values should be interpreted with caution, given the temporal resolution of NMR and the indirect nature of the comparison.

In addition to qualitative analysis, quantification of lithium deposition has also been achieved using a dedicated setup and reference spectra of metallic lithium in the same pouch cell environment as the operando experiments. The comparison with the electrochemical data reveals that, at 0 °C-2 C, more than 30% of the exchanged capacity during the CC-CV step can be attributed to plated lithium. The quantification of lithium depositions emphasizes the reversible and irreversible nature of this phenomenon. Lower temperatures exacerbate the overall deposition, but not the percentage of irreversible dead lithium, which remains on the order of 15% for the studied conditions.

The cell design developed in this study shows the possibility of extracting quantitative data on lithium plating and its dynamics on commercial-grade electrodes, although the quantitative values obtained need to be consolidated by further testing, as the experimental design remains tricky, albeit electrochemically reproducible. Other charging and discharging protocols could also be studied in the future, in order to examine their influence on the stripping of deposited lithium, by removing the CV and/or rest step at the end of the charge for example. Different discharge strategies could also be investigated to see their influence on further removal of plated lithium, reducing the overall amount of irreversible plating.

Acknowledgements

The CEA Battery FOCUS program on "Multiscale simulation of batteries applied to electrode materials" is acknowledged for the funding of the Ph.D. program of A.A. Morgane Herbomel and Yvan Reynier are thanked for the manufacturing of electrodes.

Conflict of Interest

The authors declare no conflict of interest.

Author Contributions

Abdelmounaim Akchach: conceptualization (equal); data curation (lead); formal analysis (lead); investigation (lead); validation (equal); visualization (lead); writing—original draft (lead); writing—review and editing (supporting). **Pierre-Alain Bayle:** investigation (supporting); methodology (supporting); visualization (supporting). **Anton Buzlukov:** conceptualization (supporting); investigation (supporting); validation (supporting); writing—review and editing (supporting). **Marion Chandesris:** funding acquisition (equal); investigation (supporting); methodology (supporting); validation (equal); writing—original draft (supporting); writing—review and editing (lead). **Sylvie Génies:** conceptualization (equal); data curation (supporting); funding acquisition (equal); supervision (equal); validation (equal); writing—original draft (supporting); writing—review and editing (supporting). **Michel Bardet:** conceptualization (equal); formal analysis (supporting); funding acquisition (equal); investigation (supporting); methodology (equal); supervision (equal); validation (equal); writing—original draft (supporting); writing—review and editing (supporting).

Data Availability Statement

The data that support the findings of this study are available from the corresponding author upon reasonable request.

Keywords: batteries · fast charge · graphite · lithium metal deposition · operando nuclear magnetic resonance

- [1] A. Barre, B. Deguilhem, S. Grolleau, M. Gerard, F. Suard, D. Riu, *J. Power Sources* **2013**, *241*, 680.
- [2] D. Ren, H. Hsu, R. Li, X. Feng, D. Guo, X. Han, L. Lu, X. He, S. Gao, J. Hou, Y. Li, Y. Wang, M. Ouyang, *eTransportation* **2019**, *2*, 100034.
- [3] S. Ahmed, I. Bloom, A. N. Jansen, T. Tanim, E. J. Dufek, A. Pesaran, A. Burnham, R. B. Carlson, F. Dias, K. Hardy, M. Keyser, C. Kreuzer, A. Markel, A. Meintz, C. Michelbacher, M. Mohanpurkar, P. A. Nelson, D. C. Robertson, D. Scofield, M. Shirk, T. Stephens, R. Vijayagopal, J. Zhang, *J. Power Sources* **2017**, *367*, 250.
- [4] T. Waldmann, A. Iturrondobeitia, M. Kasper, N. Ghanbari, F. Aguesse, E. Bekaert, L. Daniel, S. Genies, I. J. Gordon, M. W. Löble, E. De Vito, M. Wohlfahrt-Mehrens, *J. Electrochem. Soc.* **2016**, *163*, A2149.
- [5] J. Z. Hu, N. R. Jaegers, M. Y. Hu, K. T. Mueller, *J. Phys.: Condens. Matter* **2018**, *30*, 463001.
- [6] K. Kitada, O. Pecher, P. C. M. M. Magusin, M. F. Groh, R. S. Weatherup, C. P. Grey, *J. Am. Chem. Soc.* **2019**, *141*, 7014.
- [7] T. Waldmann, B.-I. Hogg, M. Kasper, S. Grolleau, C. G. Couceiro, K. Trad, B. P. Matadi, M. Wohlfahrt-Mehrens, *J. Electrochem. Soc.* **2016**, *163*, A1232.
- [8] A. Bichon, S. Genies, P. Azaïs, D. Buzon, O. Raccurt, *Batteries Supercaps* **2025**, 2500071, <https://doi.org/10.1002/batt.202500071>.
- [9] X. Lu, M. Lagnoni, A. Bertei, S. Das, R. E. Owen, Q. Li, K. O'Regan, A. Wade, D. P. Finegan, E. Kendrick, M. Z. Bazant, D. J. L. Brett, P. R. Shearing, *Nat. Commun.* **2023**, *14*, 5127.
- [10] A. S. Mijailovic, S. Waag-Swift, G. Wang, B. Zhou, M. Luo, W. Lu, Q. Wu, B. W. Sheldon, *Energy Environ. Sci.* **2024**, *17*, 8702.
- [11] D. P. Finegan, A. H. Quinn, D. Wragg, A. Colclasure, X. Lu, C. Tan, T. Heenan, R. Jervis, D. Brett, S. Das, T. Gao, D. Cogswell, M. Z. Bazant, M. di Michiel, S. Checchia, P. Shearing, K. Smith, *Energy Environ. Sci.* **2020**, *13*, 2570.
- [12] V. Zinth, C. von Lüders, M. Hofmann, J. Hattendorff, I. Buchberger, S. Erhard, J. Rebello-Kornmeier, A. Jossen, R. Gilles, *J. Power Sources* **2014**, *271*, 152.
- [13] C. von Lüders, V. Zinth, S. V. Erhard, P. J. Osswald, M. Hofmann, R. Gilles, A. Jossen, *J. Power Sources* **2017**, *342*, 17.

- [14] C. Hogrefe, S. Hein, T. Waldmann, T. Danner, K. Richter, A. Latz, M. Wohlfahrt-Mehrens, *J. Electrochem. Soc.* **2020**, *167*, 140546.
- [15] J. B. Lambert, E. P. Mazzola, C. D. Ridge, in *Nuclear Magnetic Resonance Spectroscopy: An Introduction to Principles, Applications, and Experimental Methods*, Wiley, Hoboken, NJ **2019**.
- [16] B. P. Matadi, S. Geniès, A. Delaillé, C. Chabrol, E. de Vito, M. Bardet, J.-F. Martin, L. Daniel, Y. Bultel, *J. Electrochem. Soc.* **2017**, *164*, A2374.
- [17] A. Buzlukov, J.-M. Mouesca, L. Buannic, S. Hediger, L. Simonin, E. Canevet, J.-F. Colin, T. Gutel, M. Bardet, *J. Phys. Chem. C* **2016**, *120*, 19049.
- [18] A. I. Freytag, A. D. Pauric, S. A. Krachkovskiy, G. R. Goward, *J. Am. Chem. Soc.* **2019**, *141*, 13758.
- [19] N. M. Trease, T. K.-J. Köster, C. P. Grey, *Electrochem. Soc. Interface* **2011**, *20*, 69.
- [20] N. M. Trease, L. Zhou, H. J. Chang, B. Y. Zhu, C. P. Grey, *Solid State Nucl. Magn. Reson.* **2012**, *42*, 62.
- [21] S. A. Kayser, A. Mester, A. Mertens, P. Jakes, R.-A. Eichel, J. Granwehr, *Phys. Chem. Chem. Phys.* **2018**, *20*, 13765.
- [22] R. L. Sacci, L. W. Gill, E. W. Hagaman, N. J. Dudney, *J. Power Sources* **2015**, *287*, 253.
- [23] K. Gotoh, T. Yamakami, I. Nishimura, H. Kometani, H. Ando, K. Hashi, T. Shimizu, H. Ishida, *J. Mater. Chem. A* **2020**, *8*, 14472.
- [24] K. Märker, C. Xu, C. P. Grey, *J. Am. Chem. Soc.* **2020**, *142*, 17447.
- [25] L. A. de Araujo, V. Sarou-Kanian, D. Sicsic, M. Deschamps, E. Salager, *J. Magn. Reson.* **2023**, *354*, 107527.
- [26] R. Wu, M. Matta, B. D. Paulsen, J. Rivnay, *Chem. Rev.* **2022**, *122*, 4493.
- [27] O. Pecher, J. Carretero-González, K. J. Griffith, C. P. Grey, *Chem. Mater.* **2017**, *29*, 213.
- [28] R. Bhattacharyya, B. Key, H. Chen, A. S. Best, A. F. Hollenkamp, C. P. Grey, *Nat. Mater.* **2010**, *9*, 504.
- [29] K. Romanenko, N. Avdievich, E. Foy, *J. Am. Chem. Soc.* **2024**, *146*, 29407.
- [30] E. Wang, M.-T. F. Rodrigues, S. Park, F. Dogan, B. Key, *J. Power Sources* **2024**, *604*, 234477.
- [31] N. Nitta, F. Wu, J. T. Lee, G. Yushin, *Mater. Today* **2015**, *18*, 252.
- [32] A. Tomaszewska, Z. Chu, X. Feng, S. O’Kane, X. Liu, J. Chen, C. Ji, E. Endler, R. Li, L. Liu, Y. Li, S. Zheng, S. Vetterlein, M. Gao, J. Du, M. Parkes, M. Ouyang, M. Marinescu, G. Offer, B. Wu, *eTransportation* **2019**, *1*, 100011.
- [33] B. Rieger, S. V. Erhard, K. Rumpf, A. Jossen, *J. Electrochem. Soc.* **2016**, *163*, A1566.
- [34] A. S. Mussa, M. Klett, G. Lindbergh, R. W. Lindstrom, *J. Power Sources* **2018**, *385*, 18.
- [35] S. Nakatoh, H. Kitagawa, Y. Kawaguchi, H. Nakamura, H. Takano, H. Tsuji, *Muscle Nerve* **1998**, *21*, 1172.
- [36] C. Eccles, *Encyclopedia of Spectroscopy and Spectrometry*, Elsevier **2017**, pp. 611–626.
- [37] B. Gruber, M. Froeling, T. Leiner, D. W. J. Klomp, *J. Magn. Reson. Imaging* **2018**, *48*, 590.
- [38] T. Yamada, A. Saito, S. Oikawa, K. Koshita, M. Takahashi, H. Maeda, S. Ohshima, *IEEE Trans. Appl. Supercond.* **2015**, *25*, 1.
- [39] Intro Model: Studying the Signal Strength of RF Coils, *COMSOL* **2023**.
- [40] C. Juchem, D. Green, R. A. de Graaf, *J. Magn. Reson.* **2013**, *236*, 95.
- [41] B. J. Walder, M. S. Conradi, J. J. Borchardt, L. C. Merrill, E. G. Sorte, E. J. Deichmann, T. M. Anderson, T. M. Alam, K. L. Harrison, *Sci. Adv.* **2021**, *7*.
- [42] Z. Guo, B. Y. Liaw, X. Qiu, L. Gao, C. Zhang, *J. Power Sources* **2015**, *274*, 957.
- [43] K. Zaghib, K. Tatsumi, Y. Sawada, S. Higuchi, H. Abe, T. Ohsaki, *J. Electrochem. Soc.* **1999**, *146*, 2784.
- [44] Y. Dai, Y. Wang, V. Eshkenazi, E. Peled, S. G. Greenbaum, *J. Electrochem. Soc.* **1998**, *145*, 1179.
- [45] B. Key, M. Morcrette, J.-M. Tarascon, C. P. Grey, *J. Am. Chem. Soc.* **2011**, *133*, 503.
- [46] N. Daumas, A. Herold, *C. R. Acad. Sci.* **1969**, *268*, 373.
- [47] J. R. Dahn, *Phys. Rev. B* **1991**, *44*, 9170.
- [48] M. Chandesris, D. Caliste, D. Jamet, P. Pochet, *J. Phys. Chem. C* **2019**, *123*, 23711.
- [49] M. Rykner, M. Chandesris, *J. Phys. Chem. C* **2022**, *126*, 5457.
- [50] M. Letellier, F. Chevallier, F. Béguin, *J. Phys. Chem. Solids* **2006**, *67*, 1228.
- [51] M. Letellier, F. Chevallier, M. Morcrette, *Carbon* **2007**, *45*, 1025.
- [52] H. S. Gutowsky, B. R. McGarvey, *J. Chem. Phys.* **1952**, *20*, 1472.
- [53] F. Holtstiege, R. Schmuck, M. Winter, G. Brunklaus, T. Placke, *J. Power Sources* **2018**, *378*, 522.
- [54] X. Lin, K. Khosravina, X. Hu, J. Li, W. Lu, *Prog. Energy Combust. Sci.* **2021**, *87*, 100953.
- [55] R. V. Bugga, M. C. Smart, *ECS Trans.* **2010**, *25*, 241.
- [56] J. C. Burns, D. A. Stevens, J. R. Dahn, *J. Electrochem. Soc.* **2015**, *162*, A959.
- [57] X. Zhao, Y. Yin, Y. Hu, S.-Y. Choe, *J. Power Sources* **2019**, *418*, 61.
- [58] I. Yoshimatsu, T. Hirai, J. Yamaki, *J. Electrochem. Soc.* **1988**, *135*, 2422.
- [59] C. von Lüders, J. Keil, M. Weersberger, A. Jossen, *J. Power Sources* **2019**, *414*, 41.
- [60] M. Petzl, M. A. Danzer, *J. Power Sources* **2014**, *254*, 80.
- [61] S. Carelli, W. G. Bessler, *J. Electrochem. Soc.* **2020**, *167*, 100515.
- [62] N. Legrand, B. Knosp, P. Desprez, F. Lapicque, *J. Power Sources* **2014**, *245*, 208.
- [63] M. W. Verbrugge, B. J. Koch, *J. Electroanal. Chem.* **1997**, *436*, 1.
- [64] T. Gao, Y. Han, D. Fragedakis, S. Das, T. Zhou, C.-N. Yeh, S. Xu, W. C. Chueh, J. Li, M. Z. Bazant, *Joule* **2021**, *5*, 393.
- [65] J. Wandt, P. Jakes, J. Granwehr, R.-A. Eichel, H. A. Gasteiger, *Mater. Today* **2018**, *21*, 231.
- [66] T. B. R. David Linden, in *Handbook of Batteries*, 3rd ed., McGraw-Hill Handbooks, McGraw-Hill, New York **2001**.

Manuscript received: March 21, 2025

Revised manuscript received: May 28, 2025

Version of record online: